

# Quantification of Efficiency Losses Due to Mobile Ions in Perovskite Solar Cells via Fast Hysteresis Measurements

Vincent M. Le Corre,\* Jonas Diekmann, Francisco Peña-Camargo, Jarla Thiesbrummel, Nurlan Tokmoldin, Emilio Gutierrez-Partida, Karol Pawel Peters, Lorena Perdigón-Toro, Moritz H. Futscher, Felix Lang, Jonathan Warby, Henry J. Snaith, Dieter Neher, and Martin Stolterfoht\*

Perovskite semiconductors differ from most inorganic and organic semiconductors due to the presence of mobile ions in the material. Although the phenomenon is intensively investigated, important questions such as the exact impact of the mobile ions on the steady-state power conversion efficiency (PCE) and stability remain. Herein, a simple method is proposed to estimate the efficiency loss due to mobile ions via “fast-hysteresis” measurements by preventing the perturbation of mobile ions out of their equilibrium position at fast scan speeds ( $\approx 1000 \text{ V s}^{-1}$ ). The “ion-free” PCE is between 1% and 3% higher than the steady-state PCE, demonstrating the importance of ion-induced losses, even in cells with low levels of hysteresis at typical scan speeds ( $\approx 100 \text{ mV s}^{-1}$ ). The hysteresis over many orders of magnitude in scan speed provides important information on the effective ion diffusion constant from the peak hysteresis position. The fast-hysteresis measurements are corroborated by transient charge extraction and capacitance measurements and numerical simulations, which confirm the experimental findings and provide important insights into the charge carrier dynamics. The proposed method to quantify PCE losses due to field screening induced by mobile ions clarifies several important experimental observations and opens up a large range of future experiments.

cells (PSCs) to reach their full potential. In particular, ion migration has been shown to be the dominant contribution to the hysteresis that is often observed in the current–voltage characteristics ( $JV$ s) of PSCs and is also thought to contribute to their instability. Many previous studies have focused their efforts not only on explaining the origin of  $JV$  hysteresis but also on setting up consistent  $JV$  measurement procedures to calculate and report efficiencies in a fair and consistent way.<sup>[1]</sup> In fact, many early reports on PSCs may have reported overestimated efficiencies by using a favorable scan direction, speed, and pre-biasing. The origin of the hysteresis feature has also been thoroughly investigated using drift-diffusion simulations showing that the appearance of hysteresis is the result of ionic motion combined with nonradiative recombination, especially when the recombination happens at the interfaces between the perovskite and the transport layers.<sup>[2–7]</sup> Experimentally,  $JV$  hysteresis has been widely studied and

assessed in perovskite solar cells; and while there are many reports of reducing  $JV$  hysteresis through: 1) compositional engineering of the perovskite absorber<sup>[8–14]</sup> or dimensionality reduction,<sup>[15–19]</sup> and 2) interfacial modification by surface


## 1. Introduction

Ionic motion in metal halide perovskites (MHPs) is one of the key challenges that needs to be overcome for perovskite solar

V. M. Le Corre, J. Diekmann, F. Peña-Camargo, N. Tokmoldin, E. Gutierrez-Partida, K. P. Peters, L. Perdigón-Toro, F. Lang, J. Warby, D. Neher, M. Stolterfoht  
Institute of Physics and Astronomy  
University of Potsdam  
14476 Potsdam-Golm, Germany  
E-mail: lecorre@uni-potsdam.de, vincent.le.corre@fau.de; stolterf@uni-potsdam.de

J. Thiesbrummel, H. J. Snaith  
Clarendon Laboratory  
Department of Physics  
University of Oxford  
Oxford OX1 3PU, UK

M. H. Futscher  
Center for Nanophotonics  
AMOLF  
1098 XG Amsterdam, The Netherlands

 The ORCID identification number(s) for the author(s) of this article can be found under <https://doi.org/10.1002/solr.202100772>.

© 2021 The Authors. Solar RRL published by Wiley-VCH GmbH. This is an open access article under the terms of the Creative Commons Attribution-NonCommercial License, which permits use, distribution and reproduction in any medium, provided the original work is properly cited and is not used for commercial purposes.

DOI: 10.1002/solr.202100772

passivation,<sup>[20–23]</sup> or 3) modification/substitution of the charge selective transport layers, it cannot be mitigated completely.<sup>[24–26]</sup> Other studies, using both AC and DC techniques were able to estimate the ion diffusion coefficient and to identify the nature and origin of the moving ions,<sup>[11,27]</sup> although the obtained diffusion coefficients typically range over several orders of magnitudes ( $10^{-6}$ – $10^{-15}$  cm<sup>2</sup> s<sup>-1</sup>) indicating different ionic species.<sup>[28–31]</sup> In the past years, halides, especially I<sup>-</sup> and Br<sup>-</sup> have often been assigned as the dominant mobile species.<sup>[32–34]</sup> However, recent reports suggest that proton diffusion may also play a major role in ion migration and should not be overlooked.<sup>[27]</sup> Hence, more work will be required to properly assign which type of ions are diffusing in the perovskite and on which timescale. Besides the ion diffusion coefficient, quantifying the actual density of moving ions remains a key challenge. Several methods have been proposed using, for example, impedance spectroscopy,<sup>[28–30]</sup> studying the current relaxation after a voltage pulse in the dark,<sup>[35–37]</sup> scanning transmission electron microscopy,<sup>[38]</sup> elemental distribution techniques,<sup>[39]</sup> or by performing numerical fits of experimental data.<sup>[40,41]</sup> Similarly to the diffusion coefficient, values for the measured ion densities vary over several orders of magnitude ( $\approx 10^{15}$  to  $10^{19}$  cm<sup>-3</sup> for polycrystalline samples) and cannot be easily assigned to a particular type of ionic species.<sup>[28,29,35,37,42]</sup> In addition, numerical simulations have shown that the influence of ions on the performance does not only depend on their density but also on the physical properties of the perovskite and the transport layers, i.e., the dielectric constant, doping density, as well as on the recombination processes and the device built-in voltage ( $V_{\text{BI}}$ ).<sup>[2,43,44]</sup> Therefore, even if the diffusion coefficient and ion density were to be measured precisely, there is currently no easy method to know how much they influence the performance of the solar cells.

Generally, the presence of a large quantity of ions is harmful to the stabilized performance of PSCs. As we will discuss later and as shown in previous reports,<sup>[2–7]</sup> the accumulation of ions at the perovskite/transport layer interfaces leads to band flattening even under short-circuit (SC) and maximum power point (MPP) conditions.<sup>[45]</sup> This band flattening causes accumulation of charges in the bulk of the perovskite, which, in turn, can dramatically increase the amount of nonradiative recombination and causes a reduction in efficiency.<sup>[2–7,45,46]</sup> To quantify the impact of ions on the *JV* characteristics, for example, to investigate the effects of optimized ion management, researchers often use the “hysteresis index” ( $\text{HI} = \text{PCE forward scan}/\text{PCE reverse scan}$ ). The HI was, however, recently challenged by Habisreutinger et al.<sup>[47]</sup> as a poor indicator of performance improvement. As previously stated, *JV* hysteresis arises from mobile ionic species in the perovskite absorber which transit through the active layer depending on the scan speed *in addition* to nonradiative recombination. It follows logically that the HI can change with: 1) a change in the amount or location of nonradiative recombination in the device; 2) a change in the ionic density; 3) a change in the ionic transit time; or 4) any combination of the previously mentioned factors. It is also clear, that a low HI also doesn't necessarily correlate with better performance. For example, *pin*-type cells display often a lower hysteresis than *nip*-type cells,<sup>[24,48]</sup> although the latter exhibit overall superior performance.<sup>[49]</sup> Furthermore, different research labs use different scan speeds to assess *JV* hysteresis which will further complicate

comparisons. It is clear that the HI is an ambiguous figure for the assessment of the impact of ions on the device.

A much more robust way to assess the performance of perovskite solar cells is to measure the steady-state power output (SPO) of the device using MPP tracking.<sup>[15,50]</sup> As the device is held at a relatively constant bias, the influence of a nonequilibrium ionic distribution on the MPP is mitigated and a more realistic picture of how it will perform under operational conditions is obtained. Resultantly, the steady-state measurement is a necessary measure in addition to a transient *JV* sweep to assess the solar cell performance parameters. However, despite the abovementioned numerical studies,<sup>[2–5]</sup> there is currently no experimental method to quantify the influence of the equilibrium ionic distribution on the steady-state performance at MPP conditions. If researchers had an unequivocal and easily measurable set of parameters to assess the impact of ions on steady-state performance this would provide many exciting new avenues of research. A strong experimental handle would make research within the field more impactful and useful toward the goal of commercially viable perovskite solar cells.

To address these important questions, we devised an easily implementable method to estimate the loss due to the ions by measuring *JV* scans, starting from open-circuit (OC) condition going to SC and back to OC, over a large scan speed range ( $10^{-3}$ – $10^3$  V s<sup>-1</sup>). Through the combination of these “fast hysteresis” measurements with drift-diffusion simulations, we showed that the efficiency at high scan speed corresponds to the efficiency in the absence of ionic contribution, i.e., the “ion-free” PCE. Hence, the efficiency difference between the fast and slow scans gives us an estimate of the loss due to the (redistribution of) mobile ions. We then investigated these ionic losses for a series of perovskites with different compositions including methylammonium lead iodide (MAPbI<sub>3</sub>), double and triple cation perovskites. We observe that the absolute PCE loss between the low and fast scan speed ranges between 1% and 3% (absolute). We complemented our study using bias-assisted charge extraction (BACE)<sup>[51]</sup> to estimate the diffusion coefficients as well as the density of the mobile ions for different perovskite compositions. These measurements demonstrated prolonged charge extraction until hundreds of ms and generally high ion densities of over  $10^{16}$  cm<sup>-3</sup> for all compositions. We also compared the obtained values with dark charge extraction by linearly increasing voltage (dark-CELIV) measurements and impedance measurements. We obtained consistent values for the diffusion coefficient for the different methods of around  $5 \times 10^{-10}$  cm<sup>2</sup> s<sup>-1</sup>. These results also highlight that the absence of *JV* hysteresis at moderate scan speeds  $< 100$  mV s<sup>-1</sup> as typically used for perovskite solar cell characterizations is not a good indicator of a negligible ion density as the peak hysteresis occurs typically at scan speeds between 1 and  $10$  V s<sup>-1</sup> for the studied *pin*-type cells. We expect that the proposed simple method to quantify the impact of mobile ions on the perovskite cell performance will be a valuable characterization tool in the future enabling the study of various aspects of this key phenomenon in perovskite solar cells.

## 2. Results

We began by investigating perovskite cells with a triple-cation Cs<sub>0.05</sub>(FA<sub>x</sub>MA<sub>y</sub>)<sub>0.95</sub>PbI<sub>x</sub>Br<sub>y</sub> composition, where  $x = 83$  and

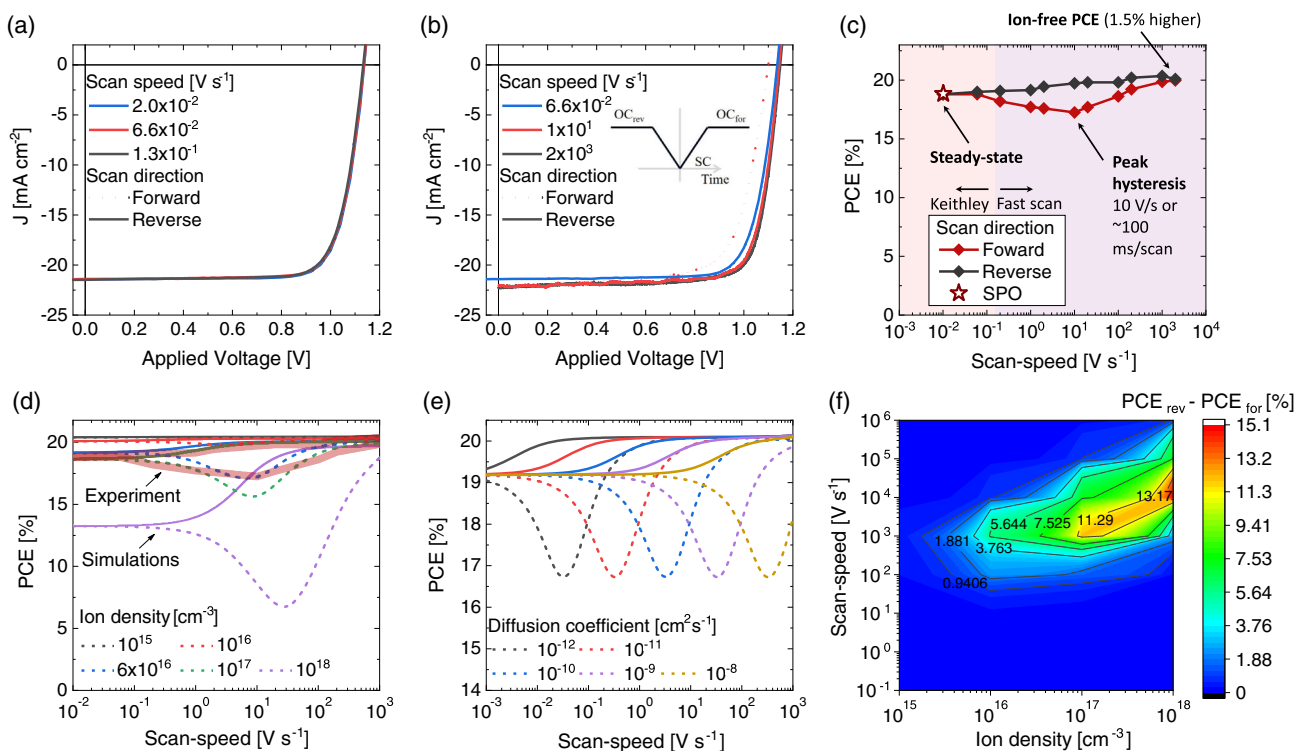


**Figure 1.** *JV* curves of a *pin*-type “83–17 triple cation” perovskite solar cell with the  $\text{Cs}_{0.05}(\text{FA}_{83}\text{MA}_{17})_{0.95}\text{PbI}_{83}\text{Br}_{17}$  composition, as measured using a) our standard setup using a Keithley 2400 and b) our custom-built setup for fast hysteresis measurements. The inset in (b) shows the measurement procedure to record the *JV* curves starting at  $V_{\text{OC}}$  to  $J_{\text{SC}}$  and back. c) The PCE from forward (0 V to  $V_{\text{OC}}$ ) and reverse ( $V_{\text{OC}}$  to 0 V) scans at different scan speeds. The PCE at the highest scan rates ( $1000 \text{ V s}^{-1}$ ) represents the PCE in the absence of ion motion, where ions cannot react anymore to the applied voltage ramp. A comparison between the PCE at fast and slow speeds (i.e., steady state) allows us to estimate the efficiency loss due to mobile ions as discussed in the main text. The experiments demonstrate a peak hysteresis at  $10 \text{ V s}^{-1}$ , which is significantly faster than accessible with a Keithley 2400. d) The simulated PCE as a function of scan speed for different ion densities in forward (dashed line) and reverse (solid line) direction. The simulations allow us to reproduce the experimental fast-hysteresis (shaded solid lines) with an ion density of  $6 \times 10^{16} \text{ cm}^{-3}$  and a diffusion coefficient of  $5 \times 10^{-10} \text{ cm}^2 \text{ s}^{-1}$ . Note, the ion density barely affects the position of the peak hysteresis. e) The simulated PCE in forward (dashed line) and reverse (solid line) direction for various ion diffusion coefficients showing the shift of the hysteresis peak. The scan speed at the peak hysteresis matches closely the transit time of ions through the active layer. f) Colormap of the difference between the reverse and forward scan PCE for varied scan speeds and ion densities, demonstrating significant PCE losses when the ion density screens the built-in field at a density of  $\approx 1 \times 10^{16} \text{ cm}^{-3}$ .

$y=17$  with the following architecture: ITO/PTAA/PFN-Br/perovskite/ $\text{C}_{60}$ /BCP/Cu. This composition typically enables the fabrication of cells with an average  $V_{\text{OC}}$  of approximately 1.13 V, a fill factor of 0.79, and a SC current density of  $21.5 \text{ mA cm}^{-2}$ , which results in a PCE of  $\approx 19.2\%$ . **Figure 1a** shows that these *pin*-type cells exhibit essentially no hysteresis at scan speeds ( $< 0.2 \text{ V s}^{-1}$ ) accessible with our standard *JV*-measurement setup. It is now widely accepted that hysteresis appears in the presence of mobile ions and charge carrier recombination.<sup>[3,4]</sup> In recent years, many reports have interpreted “hysteresis-free” *JV* curves, at moderate scan speeds, as a sign of the limited influence of the ions.<sup>[1,12,24,48,52–54]</sup> However, we will show that this is not due to a negligible influence or even absence of the mobile ions. We note that due to instrumental limitations the fastest scan speeds accessible with a Keithley 2400 (the tool typically used by researchers in the field) is usually well below  $1 \text{ V s}^{-1}$  considering a sufficiently large voltage resolution (i.e.,  $\leq 50 \text{ mV}$  per voltage step).

To overcome this limitation, we used a function generator in combination with a home-built amplifier to minimize external

resistances (see Supplementary Methods), which allowed us to measure *JV* curves at very fast scan speeds (up to  $5000 \text{ V s}^{-1}$ ). **Figure 1b** shows the *JV* curves measured at high scan speeds and **Figure 1c** summarizes the experimental PCE measured as a function of the scan speed. It is important to note that we started the *JV* scans from OC to (SC conditions in the reverse direction and back from SC to OC in the forward direction. As illustrated in the inset of **Figure 1b**, this will be the standard *JV*-scan measurement method throughout the manuscript unless specified otherwise. The results demonstrate a maximum amplitude of the hysteresis at scan speeds of  $\approx 10 \text{ V s}^{-1}$  (or  $\approx 100 \text{ ms}$  per scan), while the hysteresis is absent at lower and significantly higher scan speeds.<sup>[44]</sup> As we will demonstrate in detail in this manuscript, the PCE at the fastest scan speeds is approximately equal to the PCE in the absence of mobile ions. Hence, one can use the point at high scan speeds where the forward and reverse scan merge again to estimate the “ion-free” PCE and the difference between the steady-state PCE (i.e., at low scan speed) and the fast scan to determine the losses due to the mobile ions. For the 83–17 triple cation composition,

we quantify an efficiency loss of ca. 1.5% due to the presence of mobile ions. It is important to note that the high scan-speed PCE can be used as a measure for the “ion-free” PCE only when the ions are roughly homogeneously distributed in the bulk of the perovskite. This is the case if the built-in voltage ( $V_{\text{BI}}$ ) in the device is offset by the applied voltage. However, at prebiases different to the  $V_{\text{BI}}$ , the ions accumulate at the interface, which will cause an overestimation of the “ion-free” efficiency at forward biases  $>V_{\text{BI}}$ , or an underestimation in the case of smaller prebiases. This is shown in Supplementary Figure S1a,b and all experimental details are provided in the Supplementary Methods. Although the built-in voltage is in general not precisely known, we have recently shown that the high device fill factor and  $V_{\text{OC}}$  cannot be reproduced with built-in voltages lower than 1 V.<sup>[46]</sup> This is also consistent with capacitance versus voltage measurements, which demonstrate a  $V_{\text{BI}}$  close to the device  $V_{\text{OC}}$  of the triple cation device (Supplementary Figure S1c). Therefore, using the  $V_{\text{OC}}$  as a prebias closely reflects the ion-free efficiency and also allows for a simple comparison of the devices under well-defined starting conditions. It is further important to note that the ionic loss from fast to slow scan speeds directly impacts the SPO of the cell. This can be seen when the MPP is tracked with a high time resolution ( $\approx 10$  ms, Supplementary Figure S2), which highlights a significantly higher power output on the sub-second timescales. The SPO from the MPP tracking at longer times ( $\approx 100$  s) is plotted with a star symbol in Figure 1c, which shows that its value is essentially identical to the PCE measured at slow scan speeds ( $<100$  mV s<sup>-1</sup>). Finally, as a reference measurement for a material without moving ions, we also performed the fast-hysteresis measurements on an organic solar cell, made of a well-known PM6:Y6 blend, and as expected we do not see a hysteresis nor a difference between the PCE at fast and slow scan speeds on the studied timescales as shown in Supplementary Figure S3a. To confirm that the observed hysteresis is indeed caused by the ionic redistribution and not by any trapping/detrapping processes, we also measured an 83-17 triple cation *pin*-type cell at different temperatures (RT, 250 and 200 K), see Supplementary Figure S3b. As expected from a reduction of the ionic mobility with decreasing temperature, we see a clear shift of the maximum hysteresis feature to slower scan speeds. We also observed that the hysteresis is essentially absent at low temperatures within the measured scan speed range, especially at high scan speeds where hysteresis could appear due to trapping/detrapping. This indicates that trapping/detrapping is not the primary cause of the hysteresis.

To further investigate the effect of ions and to reproduce our experimental hysteresis results, we used the open-source drift-diffusion package IonMonger.<sup>[41]</sup> The parameters used in the simulations and shown in the Supplementary Information, Table S1, are mostly based on our previous reports.<sup>[46]</sup> In these studies, we were already able to reproduce several experimental results such as the ideality factor, the measured bulk and interfacial recombination currents,<sup>[55]</sup> using experimental input from transient photoluminescence (PL) measurements, such as interface recombination velocities and bulk lifetimes. Interestingly, as shown in Figure 1d, we were able to reproduce the fast-hysteresis measurements with an ion density of  $6 \times 10^{16}$  cm<sup>-3</sup> and a diffusion coefficient of  $5 \times 10^{-10}$  cm<sup>2</sup> s<sup>-1</sup>, which is consistent with our charge extraction measurements as discussed in the

following section. Note that in the simulations we only considered mobile cations while the anions remain fixed. However, we emphasize that we cannot exclude that there might be other simulation settings that would reproduce the fast-hysteresis measurements and the experiments shown in our previous work<sup>[46]</sup> with different ion densities, since the effect of the mobile ion density depends on several devices and material parameters as mentioned in the introduction. Moreover, it should be noted that the absolute values may differ due to the multifarious device and material parameters which influence the model. Nevertheless, trends can be reliably investigated using these simulations.

Motivated by the successful reproduction of experimental observation by the simulations, we varied the ion density (Figure 1d) and diffusion coefficient (Figure 1e) to study the effect on the *JV* curves and the PCE difference between the forward and reverse scan. As discovered earlier by others,<sup>[44]</sup> we see that the hysteresis is absent at fast and slow scan speeds. Moreover, the timescale at which the maximum *JV* hysteresis (which we call “peak hysteresis”) occurs, appears to depend primarily on the ion diffusion coefficient (the larger  $D_{\text{ion}}$  the higher the scan speed to resolve the maximum hysteresis) and to a lesser degree on the ion density. In fact, when we plot the transit time of the ions as obtained from the ion mobility, we find a near-perfect agreement between the scan speed time and the ion transit time through the active layer. This is shown in Supplementary Figure S4. Hence, the scan time at the maximum hysteresis is roughly equal to the transit time of ions through the active layer. Therefore, the peak hysteresis can be used as an approximate measure of the effective ion speed,<sup>[56]</sup> although we note that there might be other device and material parameters that cause a deviation from this agreement, which need to be further investigated in the future. Figure 1f shows the difference between reverse and forward PCE as a function of scan speed and ion density. While the PCE is not strongly affected by the scan speed at low ion densities, for ion densities  $>10^{16}$  cm<sup>-3</sup> the PCE is low for slow scan rates but remains high at fast scan rates. It is also important to note that a significant hysteresis will only appear if the ion density is large enough to screen (or more precisely “redistribute”) the built-in field. A high  $V_{\text{BI}}$  is necessary to achieve a high performance in perovskite solar cells.<sup>[57]</sup> This is the case if  $n_{\text{ion}}$  is approximately equal to or larger than the charge on the electrodes per cell volume ( $CV_{\text{BI}}/eV_{\text{ol}} \approx 10^{16}$  cm<sup>-3</sup>, where  $C$  is the geometrical capacitance,  $e$  the elementary charge, and  $V_{\text{ol}}$  the volume of the cell). Therefore, regardless of the scan speed, Figure 1d,f shows a significant hysteresis only from ion densities of approximately  $10^{16}$  cm<sup>-3</sup> or above. Figure 1d,f also show that the PCE loss at small scan speeds strongly depends on the ion density but is not affected by the ionic diffusion coefficient, which only shifts the position of the peak hysteresis on the x-axis.

Having observed the profound effect of ion density and diffusion coefficient, we aim to better explain the scan-speed-dependent hysteresis via the energy bands and accumulation of the ions depending on the scan speed and direction and the device operating point. We note again that the voltage sweep is again performed from OC to SC and back to OC as exemplified in Figure 2a. The corresponding PCE as a function of scan speed and direction is shown in Figure 2b, while Figure 2c shows the *JV* curves at the characteristic scan speeds (slow, medium, and fast as pointed out in Figure 2b). The corresponding *JV* curves

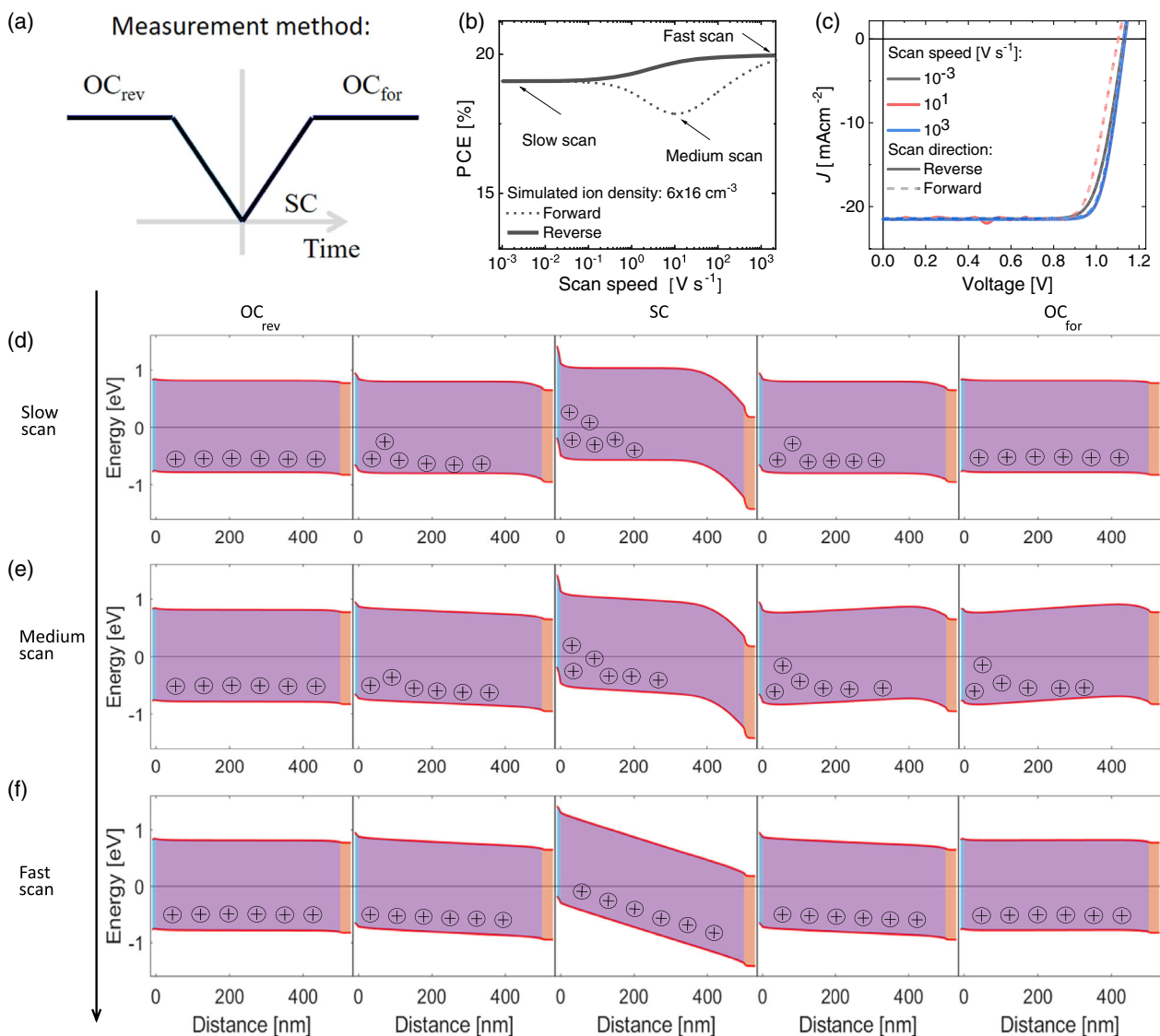


**Figure 2.** a) The measurement procedure to record the  $JV$  curves and band diagrams starting at  $V_{OC}$  to  $J_{SC}$  and back. Panel (b) highlights the simulated fast-hysteresis PCE plot in forward and reverse scan and the characteristic efficiencies at slow, medium and fast scan speeds. Panel (c) shows the corresponding simulated  $JV$  curves. Panel (d–f) shows the corresponding energy diagrams at the characteristic: d) slow, e) medium, and f) fast scan speed as marked in panel (b) in chronological order: the initial OC condition, then the MPP of the reverse scan  $\approx 0.9$  V, SC, and then back to 0.9 V and again to OC. Note, the mobile ions are considered to be positively charged halide vacancies, while the negatively charged counter ions stay uniformly distributed in the active layer (not shown).

and recombination currents (bulk, interface, contacts) for each condition are provided in Supplementary Figure S5. At low scan speeds compared to the speed of ions (i.e., at quasi-steady-state conditions), by sweeping from OC to SC, the ions have sufficient time to move and accumulate at the interfaces at each incremental voltage step. This scenario is exemplified by the band diagrams in Figure 2d. At SC, the accumulation of net ionic charges at the interfaces leads to field-free regions in the perovskite bulk (Figure 2d), which also persists during the forward scan at high enough scan speeds. It is important to note that the mobile ion density does not entirely screen the  $V_{BI}$ , but redistributes it, leading to the formation of a field-free region and a

broad space charge region in the active layer, as well as stronger fields at the interfaces where the mobile ions accumulate as compared to the mobile-ion-free case. We note that the space charge region in the active layer is due to the presence of homogeneously distributed, immobile counter ions in the active layer. The field-free regions in turn increase predominately the non-radiative recombination in the bulk, since the carrier density is increased in that region, but also at the  $p$ -interface as compared to the ion-free case. The recombination currents (bulk, interface, contacts) at each condition are depicted in Supplementary Figure S5, while Supplementary Figure S6 shows the accumulation of ions. At intermediate scan speeds,

where the ion speed is approximately equal to the scan speed, the peak hysteresis is observed. This scenario is exemplified by the band diagrams in Figure 2e and occurs when the ions slightly lag behind the scan speed and thus do not have time to move back during the forward scan and remain in a position close to their SC position during the forward scan. This creates a pit in the energy band and a negative field region (in particular at the MPP in the forward scan), which in turn can dramatically reduce the efficiency due to less efficient charge extraction. Finally, at the *fastest scan speeds*, much larger than the ion speed, the ions have no time to react and remain locked in their initial position under OC conditions. This scenario is exemplified by the band diagrams in Figure 2f. Since the ions have no time to react to the change in the external electric field, they do not significantly impact the device performance as the formation of field-free regions is prevented (which reduces the recombination).

In the next paragraph, we aim to corroborate the previously fast-hysteresis measurements with complementary charge extraction measurements. To this end, we first estimated the density of mobile ions and their extraction time via BACE measurements in the dark.<sup>[51]</sup> Briefly in the measurement, the cell is kept at “OC-like” condition. For this measurement, we define the OC condition as the point at which the injection current equals the  $J_{SC}$ , which takes into account possible voltage losses over device and external resistances, which reduce the actual voltage

drop over the device in the dark. Then, the voltage is switched to a collection bias ( $V_{coll}$ ), in this case, 0 V. Upon switching the voltage, the carriers present in the device get extracted allowing us to estimate the carrier density by integrating the current. We also note that the mobile ions are not “extracted” out of the device per se rather *transported* to the perovskite/transport layer interfaces (or even metal contacts). The movement of ionic charge toward the interfaces at SC conditions leads to a displacement current in the external circuit, which is equivalent to the ionic current. By plotting the current in Figure 3a and the integral of the current in Figure 3b, i.e., the extracted charge on a log-log scale, we observe two distinct regimes in the current decay. The first regime in the  $\mu$ s-regime corresponds to the RC-discharge of the metal electrodes (“CU charge”) and the extraction of fast-moving electronic charges that have been injected into the cell upon application of the forward bias. The second regime corresponds to slow-moving charges, which we assign to the mobile ions in the ms-regime. The first plateau shows an extracted charge of  $\approx 1.5 \times 10^{16} \text{ cm}^{-3}$  after less than  $\approx 1 \mu\text{s}$ . Through the application of a reference voltage step from 0 V to minus  $V_{OC}$ , we can disentangle the contribution of the capacitive charge and electronic injected charge to the first plateau as it is done routinely for organic solar cells.<sup>[58]</sup> Supplementary Figure S7 shows that the capacitive charge contributes the larger fraction ( $\approx 1 \times 10^{16} \text{ cm}^{-3}$ ) to the first charge plateau than the electronic injected charge ( $\approx 5 \times 10^{15} \text{ cm}^{-3}$ ). The first charge

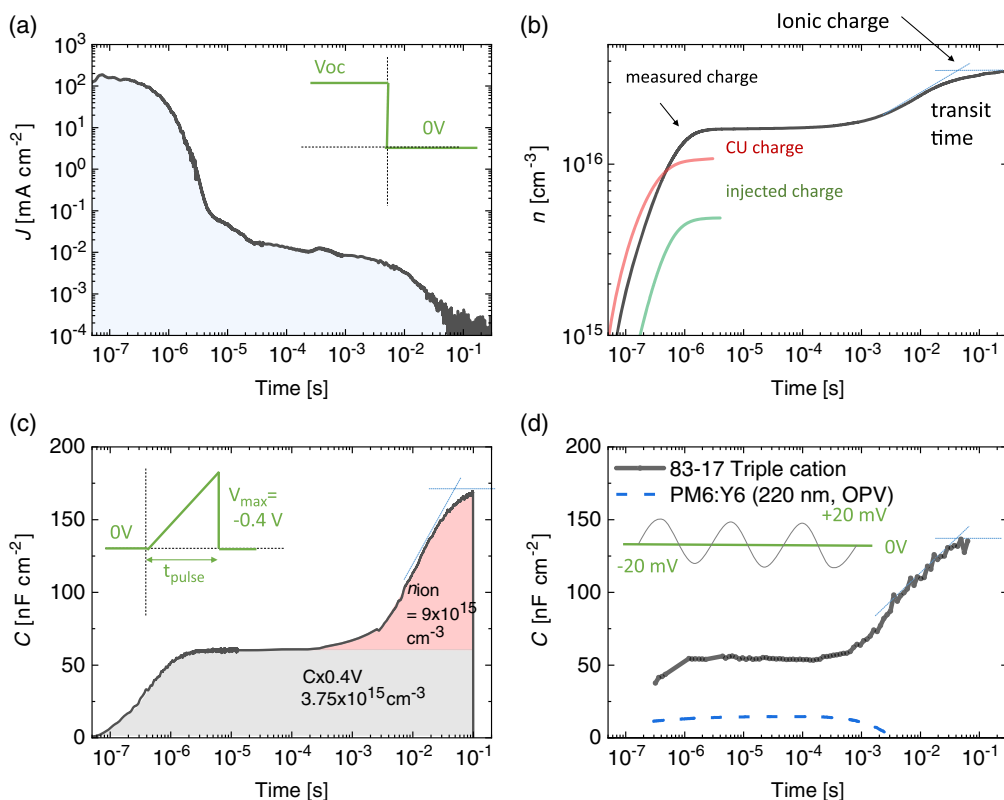


**Figure 3.** a) BACE, b) integrated BACE, c) charge extraction by linearly increasing voltage in the dark (dark-CELIV), and d) capacitance versus frequency, all performed in the dark for the 83-17 triple cation perovskite device, showing a consistent signal for the ions in the ms – s regime. The dashed blue line in (d) represents a PM6:Y6 organic solar cell, which shows no signal at long timescales (i.e., low frequencies) where the ionic signal is seen for perovskite. The dashed straight lines indicate the estimated ion-transit times from each measurement.

extraction regime is then followed by a plateau of the extracted charge, until approximately 1 ms where the extracted charge rises again due to the displacement of mobile ions in the internal field. Surprisingly, the second extraction regime occurs between 1 ms and  $\approx 100$  ms and peaks at an extracted charge of  $\approx 3.5 \times 10^{16} \text{ cm}^{-3}$ . We determine the characteristic ion transit time from the saturation of the extracted charge at around 60 ms. Considering the whole active layer as the diffusion length, this results in an effective ion mobility of  $2 \times 10^{-8} \text{ cm}^2 \text{ V}^{-1} \text{ s}^{-1}$  and a diffusion constant of  $5 \times 10^{-10} \text{ cm}^2 \text{ s}^{-1}$  at room temperature, which fits the diffusion constant obtained from the fit of the fast hysteresis ( $5 \times 10^{-10} \text{ cm}^2 \text{ s}^{-1}$ ). By subtracting the capacitive and injected electronic charge (i.e., the first rise/bump) from the total integrated charge, we can consequently estimate the ionic charge to be  $\approx 2 \times 10^{16} \text{ cm}^{-3}$ . Clearly, the capacitive and injected electronic charge contribution is smaller than the signal from the mobile ions, which highlights their importance. We also note that we checked the extraction of mobile ions on even longer timescales (from 0.3 to 100 s) with a Keithley 2400, however, an insignificant additional ion density was obtained (Supplementary Figure S8). Nevertheless, it is important to note that the extracted ionic density might be underestimated due to two reasons. First, if the initial ion distribution deviates from a uniform distribution, this can lead to an underestimation of the charge in the active layer. Second, and more importantly, the final ionic distribution needs to be taken into account. Considering that the extracted ionic charge is larger than the charge on the electrodes ( $CV_{\text{BI}}$ ) creating the built-in field, the formation of field-free regions is expected during the BACE measurement. This would inhibit further ionic transport and the displacement current goes to zero, which would also lead to an underestimation of the ionic charge. To understand the limitation to field screening in the BACE measurement, we first tried to increase the collection voltage between  $-1.6 \text{ V} < V_{\text{coll}} < 0$ , which increases the field in the active layer. However, as shown in Supplementary Figure S9, the extracted charge could not be saturated with increasing reverse bias. Therefore, at this point, although inconsistent with our simulations, we do not exclude that higher ion densities might be present in the device due to the experimental uncertainties. However, this is beyond the scope of the present article.

To further corroborate the BACE measurements experimentally, we also performed charge extraction by linearly increasing voltage (dark-CELIV) and capacitance versus frequency (Cf) impedance measurements as shown in Figure 3c,d, while the biasing conditions are highlighted in the insets, respectively. We note that the change in capacitance is again related to the transport of ionic charge toward the edges in the active layer which increases the capacitance.<sup>[30,59]</sup> Interestingly, both measurements demonstrate a qualitatively similar shape as observed in BACE, i.e., an initial shoulder to the capacitive step and extraction of electronic charges, which is then followed by a rise due to the transport of mobile ions starting at several hundred  $\mu\text{s}$ . Moreover, the saturation of the signal begins in both measurements at several tens of ms, which is consistent with the BACE measurement and the obtained effective ion diffusion coefficient. However, we note that the obtained ionic charge in dark-CELIV ( $9 \times 10^{15} \text{ cm}^{-3}$ ) is smaller than in BACE (see Figure 3c and Supplementary Figure S10 for more information

on how to calculate the capacitance from dark-CELIV measurements). This might be because dark-CELIV and Cf measurements start at SC conditions initially, while BACE starts at OC conditions, hence the mobile ions might be transported over smaller distances as in dark-CELIV (and Cf) as compared to BACE, or because the change in applied voltage is smaller in dark-CELIV (and Cf). Another potential limitation of impedance spectroscopy for the study of ion movement lies in the difficulty of performing the measurements at sufficiently low frequencies while maintaining device stability and a reasonable signal-to-noise ratio. In addition, the extracted capacitance signal in the Cf (and dark-CELIV) measurements will depend on the applied voltage and illumination intensity,<sup>[60,61]</sup> complicating the determination of the respective amount of probed charges and its correlation with the BACE measurement. Finally, attribution of the lower frequency response for the impedance measurements in the literature has not been unanimous, with such processes as trapping and detrapping of carriers<sup>[62,63]</sup> proposed, in addition to the ion movement and resulting charge accumulation at the contacts.<sup>[61]</sup> Nevertheless, our complimentary set of measurements and simulations highlight that there are a large number of ions present in the active layer, which leads to the formation of field-free regions and links the timescales observed in the fast-hysteresis measurement to the extraction time of ions.

In the next paragraph, we aimed to generalize our findings to other perovskite systems. To this end, the same set of measurements was performed on six different perovskite compositions pure  $\text{MAPbI}_3$ , a double cation perovskite  $\text{Cs}_{0.15}\text{FA}_{0.85}\text{PbI}_{75}\text{Br}_{25}$  which is popular for applications in tandem solar cells due to its bandgap of 1.7 eV and three triple cation perovskites ( $\text{Cs}_{0.05}(\text{FA}_x\text{MA}_y)_{0.95}\text{PbI}_x\text{Br}_y$ ). The same architecture as introduced previously (ITO/PTAA/PFN-Br/perovskite/ $\text{C}_{60}$ /BCP/Cu) was used for all the devices. The characteristic JV parameters for each system are plotted in Supplementary Figure S11. Figure 4a summarizes the fast-hysteresis measurements, which show that the peak hysteresis occurs on similar timescales for all compositions, i.e., around  $\approx 1$  to  $10 \text{ V s}^{-1}$ . The estimated PCE losses due to mobile ions are shown in Figure 4b for the different perovskite compositions. Interestingly, in all cases, 1–3% (absolute) of the PCE is lost as a result of the field screening due to mobile ions. Interestingly, when the relative content of  $\text{MAPbBr}_3$  is varied with respect to  $\text{FAPbI}_3$ , the lowest relative ionic loss is observed in the most efficient 83–17 perovskite. This is then followed by the 95–5, 60–40 triple cation and 100:0 perovskite, which follows the trend in efficiency (Supplementary Figure S11). Moreover, we found that the relative ionic loss increases from the mono cation perovskite ( $\text{MAPbI}_3$ ) to the double cation perovskite ( $\text{Cs}_{0.15}\text{FA}_{0.85}\text{PbI}_{75}\text{Br}_{25}$ ) and the triple cation perovskites ( $\text{Cs}_{0.05}(\text{FA}_{83}\text{MA}_{17})_{0.95}\text{PbI}_{83}\text{Br}_{17}$ ). Nevertheless, despite these differences, overall, the results for different perovskites are fairly similar, which points to common dominant ionic species being present in each device. We also analyzed how the PCE loss due to ions impacts the individual JV parameters. Supplementary Figure S12, exemplifies the measured PCE parameter versus scan rate for the 83-17 triple cation perovskite. Importantly, as shown in Figure 4c, the relative PCE loss due to the mobile ions is primarily a result of a reduced  $J_{\text{SC}}$  rather than the FF. Also, the rate-dependent  $V_{\text{OC}}$  is affected by the ionic distribution especially at medium scan speed where the

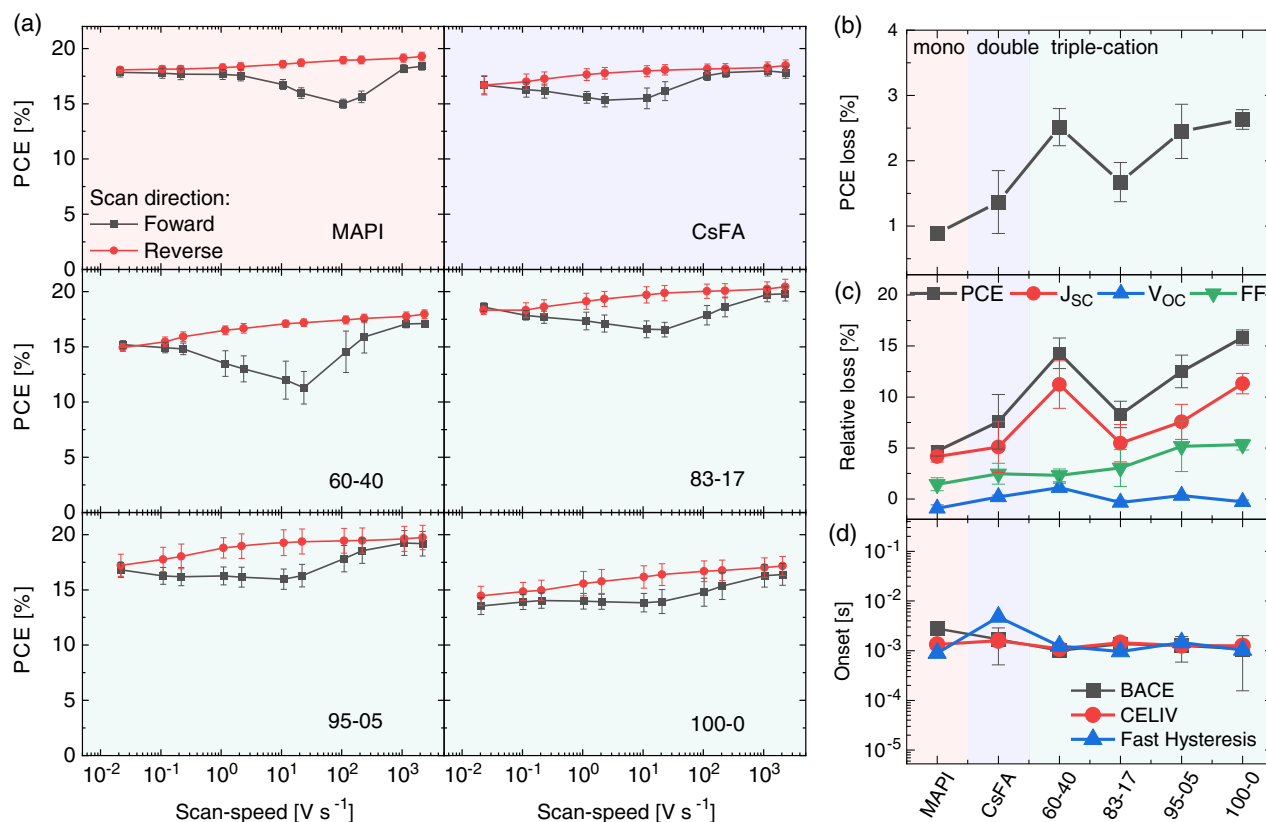


**Figure 4.** a) Fast-hysteresis measurements measured for different perovskite compositions in a *pin*-structure as highlighted in each panel. Note, that for triple cation perovskites with a composition of  $\text{Cs}_{0.05}(\text{FA}_x\text{MA}_y)_{0.95}\text{PbI}_x\text{Br}_y$ , the ratio of  $x$  to  $y$  is specified in each panel. b) The absolute PCE loss due to the mobile ions for the different compositions as estimated from the difference between the PCE at fast and slow scan speeds. c) A breakdown of the relative losses in each *JV* parameter for all compositions. Interestingly, for all compositions, the effect of the ions is primarily on the SC current, while the OC voltage is barely affected by the presence of the mobile ions and the formation of the field-free regions. d) A comparison of the onset of the ionic signal as obtained from BACE, charge extraction by linearly increasing the voltage in the dark (dark CELIV), and the onset of the fast-hysteresis at short-timescales.

accumulation of ions near the TL interface leads to overall increased recombination. However, and somewhat surprisingly to us, as shown in Supplementary Figure S12, the  $V_{\text{OC}}$  loss between slow and fast scan is relatively small since the applied bias is here high enough to compensate for the  $V_{\text{BI}}$  and redistribute ions within the bulk of the perovskite giving very similar condition as seen in the band diagram in Figure 2 and in the experiments. We note that the data has been acquired on at least five cells for each composition, which have been stored in the glovebox for several days. We believe that the future modeling of these results will further contribute to understanding the band structure of perovskite solar cells in the presence of large amounts of mobile ions. Supplementary Figures S13 and S14 show the dark-CELIV and BACE measurements for all compositions. Also, these measurements indicate similar trends. For example, the onset of the ionic signal in the BACE, dark-CELIV, and impedance, which could be considered as an estimate of the fastest ionic species, is similar in all samples. As shown in Figure 4d, for all three experiments, the onset starts in the ms regime ( $\approx 1$  ms in dark-CELIV and Cf and around 10 ms in fast-hysteresis).

Finally, to further highlight the potential of the fast-hysteresis measurements, we measured a double cation

$\text{Cs}_{0.15}\text{FA}_{0.85}\text{PbI}_{75}\text{Br}_{25}$  *pin*-type perovskite cell that we intentionally degraded upon illumination for several hours under OC conditions with a white light-emitting diode (and a 1 sun equivalent intensity, without UV). As demonstrated in Supplementary Figure S15, for this cell, we observed a large increase of the ion-induced loss from  $\approx 1.4\%$  to  $\approx 6\%$  (absolute). This highlights the importance of mobile ions in the degradation process in perovskite solar cells and also the usefulness of the proposed methodology to study the main degradation mechanism in perovskite solar cells by enabling an independent assessment of the steady-state and the ion-free PCE.

### 3. Conclusion

In summary, we proposed a simple method to estimate the efficiency loss due to the presence of mobile ions via fast-hysteresis measurements. These measurements can be performed in addition to the standard *JV* characterization of cells with a Keithley SMU. The quantification of the ion-free PCE was achieved by offsetting the device's internal voltage and performing a fast hysteresis scan before the ions can react to the change in the internal



field. By doing numerical simulations, we were able to explain all three main features in the fast-hysteresis, i.e., the steady-state performance, the peak hysteresis, and the ion-free PCE. By plotting the band structure and ion distributions as a function of scan rate, scan direction, and operating condition, we could explain why the peak hysteresis appears when the scan speed is close to the effective speed of the mobile ions. If the response of the ions lags somewhat behind the change in the external bias, a large amount of ions accumulates at the edges of the active layer in the forward scan direction, in particular at the MPP, which significantly lowers the PCE at this particular scan speed. We then performed transient charge extraction measurements (BACE, dark-CELIV, and capacitance versus frequency) to correlate the kinetics of mobile ions and their density to the peak hysteresis. Although the different biasing conditions need to be taken into account in these measurements, they all demonstrated a significant ionic redistribution in the active layer after several 100  $\mu\text{s}$  which lasts to the second timescales. Moreover, BACE measurements demonstrated a high ionic density in the active layer of at least  $2 \times 10^{16} \text{ cm}^{-3}$ , which is larger than the charge on the electrodes per cell volume ( $\approx 1 \times 10^{16} \text{ cm}^{-3}$ ) and the injected carrier density at  $V_{OC}$  ( $\approx 5 \times 10^{15} \text{ cm}^{-3}$ ). Finally, the fast-hysteresis and transient extraction measurements were extended to a range of different perovskite compositions, which highlights subtle differences in the loss due to mobile ions and extraction times, although the differences between the different compositions were smaller than expected. The proposed simple method to quantify the losses due to mobile ions will open up a range of future experiments to study the impact of various aspects on the ionic losses, such as the cell architecture, transport layers, and additives or aging. However, more efforts are required to precisely quantify the device internal voltage in the future. This will generate new insights into these key phenomena in perovskite solar cells. Our results also highlight that further efficiency improvements are still possible through further reduction of the density of mobile ionic species in the metal halide perovskites.

## Supporting Information

Supporting Information is available from the Wiley Online Library or from the author.

## Acknowledgements

The authors acknowledge funding from the Deutsche Forschungsgemeinschaft (DFG, German Research Foundation) within the SPP 2196 (SURPRISE 423749265 and HIPSTER 424709669). The authors further acknowledge financial support by the Federal Ministry for Economic Affairs and Energy within the framework of the 7th Energy Research Programme (P3T-HOPE, 03EE1017C) and HyPerCells (a joint graduate school of the Potsdam University and the HZB). F.L. acknowledges financial support from the Alexander von Humboldt Foundation via the Feodor Lynen program. The work of M.H.F. is funded by The Netherlands Organisation for Scientific Research (NWO). The authors also thank Dr. Nicola Courtier for her kind support with IonMonger.

Open access funding enabled and organized by Projekt DEAL.

## Conflict of Interest

H.J.S. is co-founder and CSO of Oxford PV Ltd., a company commercializing perovskite PV technology.

## Data Availability Statement

The data that support the findings of this study are available from the corresponding author upon reasonable request.

## Keywords

hysteresis, mobile ions, perovskite solar cells

Received: September 22, 2021

Revised: December 10, 2021

Published online:

- [1] J. A. Christians, J. S. Manser, P. V. Kamat, *J. Phys. Chem. Lett.* **2015**, *6*, 852.
- [2] N. E. Courtier, J. M. Cave, J. M. Foster, A. B. Walker, G. Richardson, *Energy Environ. Sci.* **2019**, *12*, 396.
- [3] T. S. Sherkar, C. Momblona, L. Gil-Escrig, J. Ávila, M. Sessolo, H. J. Bolink, L. J. A. Koster, *ACS Energy Lett.* **2017**, *2*, 1214.
- [4] G. Richardson, S. E. J. O'Kane, R. G. Niemann, T. A. Peltola, J. M. Foster, P. J. Cameron, A. B. Walker, *Energy Environ. Sci.* **2016**, *9*, 1476.
- [5] T. S. Sherkar, C. Momblona, L. Gil-Escrig, H. J. Bolink, L. J. A. Koster, *Adv. Energy Mater.* **2017**, *7*, 1602432.
- [6] P. Calado, A. M. Telford, D. Bryant, X. Li, J. Nelson, B. C. O'Regan, P. R. F. Barnes, B. C. O'Regan, P. R. F. Barnes, *Nat. Commun.* **2016**, *7*, 13831.
- [7] W. Tress, N. Marinova, T. Moehl, S. M. Zakeeruddin, M. K. Nazeeruddin, M. Grätzel, *Energy Environ. Sci.* **2015**, *8*, 995.
- [8] D. Y. Son, S. G. Kim, J. Y. Seo, S. H. Lee, H. Shin, D. Lee, N. G. Park, *J. Am. Chem. Soc.* **2018**, *140*, 1358.
- [9] J. Liu, Q. Han, Y. Bai, K. Z. Du, T. Li, D. Ji, Y. Zhou, C. Cao, D. Shin, J. Ding, A. D. Franklin, J. T. Glass, J. Hu, M. J. Therien, D. B. Mitzi, *Energy Environ. Sci.* **2017**, *10*, 2365.
- [10] M. Sun, F. Zhang, H. Liu, X. Li, Y. Xiao, S. Wang, *J. Mater. Chem. A* **2017**, *5*, 13448.
- [11] L. McGovern, I. Koschany, G. Grimaldi, L. A. Muscarella, B. Ehrler, *J. Phys. Chem. Lett.* **2021**, *12*, 2423.
- [12] C. Geffroy, E. Grana, T. Bessho, S. Almosni, Z. Tang, A. Sharma, T. Kinoshita, F. Awai, E. Cloutet, T. Toupance, H. Segawa, G. Hadziioannou, *ACS Appl. Energy Mater.* **2020**, *3*, 1393.
- [13] S. Bai, P. Da, C. Li, Z. Wang, Z. Yuan, F. Fu, M. Kawecki, X. Liu, N. Sakai, J. T.-W. Wang, S. Huettner, S. Buecheler, M. Fahlman, F. Gao, H. J. Snaith, *Nature* **2019**, *571*, 245.
- [14] S.-G. Kim, C. Li, A. Guerrero, J.-M. Yang, Y. Zhong, J. Bisquert, S. Huettner, N.-G. Park, *J. Mater. Chem. A* **2019**, *7*, 18807.
- [15] Z. Wang, Q. Lin, F. P. Chmiel, N. Sakai, L. M. Herz, H. J. Snaith, *Nat. Energy* **2017**, *2*, 17135.
- [16] Y. Zhang, F. Liu, C. Jiang, F. Tang, X. Zhang, *J. Mater. Chem. C* **2021**, *9*, 3470.
- [17] T. Niu, H. Ren, B. Wu, Y. Xia, X. Xie, Y. Yang, X. Gao, Y. Chen, W. Huang, *J. Phys. Chem. Lett.* **2019**, *10*, 2349.
- [18] J. Yuan, Y. Jiang, T. He, G. Shi, Z. Fan, M. Yuan, *Sci. China Chem.* **2019**, *62*, 629.
- [19] Y. Lin, Y. Bai, Y. Fang, Q. Wang, Y. Deng, J. Huang, *ACS Energy Lett.* **2017**, *2*, 1571.

- [20] S. G. Kim, J. Chen, J. Y. Seo, D. H. Kang, N. G. Park, *ACS Appl. Mater. Interfaces* **2018**, *10*, 25372.
- [21] Q. Jiang, Y. Zhao, X. Zhang, X. Yang, Y. Chen, Z. Chu, Q. Ye, X. Li, Z. Yin, J. You, *Nat. Photonics* **2019**, *13*, 460.
- [22] C. Zhang, H. Wang, H. Li, Q. Zhuang, C. Gong, X. Hu, W. Cai, S. Zhao, J. Chen, Z. Zang, *J. Energy Chem.* **2021**, <https://doi.org/10.1016/j.jechem.2021.07.011>.
- [23] M. Wang, W. Li, H. Wang, K. Yang, X. Hu, K. Sun, S. Lu, Z. Zang, *Adv. Electron. Mater.* **2020**, *6*, 2000604.
- [24] H. S. Kim, I. H. Jang, N. Ahn, M. Choi, A. Guerrero, J. Bisquert, N. G. Park, *J. Phys. Chem. Lett.* **2015**, *6*, 4633.
- [25] T. Bu, J. Li, F. Zheng, W. Chen, X. Wen, Z. Ku, Y. Peng, J. Zhong, Y. B. Cheng, F. Huang, *Nat. Commun.* **2018**, *9*, 4609.
- [26] F. Giordano, A. Abate, J. P. Correa Baena, M. Saliba, T. Matsui, S. H. Im, S. M. Zakeeruddin, M. K. Nazeeruddin, A. Hagfeldt, M. Graetzel, *Nat. Commun.* **2016**, *7*, 10379.
- [27] D. R. Ceratti, A. Zohar, R. Kozlov, H. Dong, G. Uraltsev, O. Girshevitz, I. Pinkas, L. Avram, G. Hodes, D. Cahen, *Adv. Mater.* **2020**, *32*, 2002467.
- [28] M. H. Futscher, J. M. Lee, L. McGovern, L. A. Muscarella, T. Wang, M. I. Haider, A. Fakharuddin, L. Schmidt-Mende, B. Ehrler, *Mater. Horizons* **2019**, *6*, 1497.
- [29] S. Reichert, J. Flemming, Q. An, Y. Vaynzof, J.-F. Pietschmann, C. Deibel, *Phys. Rev. Appl.* **2020**, *13*, 034018.
- [30] O. Almora, I. Zarazua, E. Mas-Marza, I. Mora-Sero, J. Bisquert, G. Garcia-Belmonte, *J. Phys. Chem. Lett.* **2015**, *6*, 1645.
- [31] Akriti, S. Zhang, Z.-Y. Lin, E. Shi, B. P. Finkenauer, Y. Gao, A. J. Pistone, K. Ma, B. M. Savoie, L. Dou, *Adv. Mater.* **2021**, 2105183.
- [32] T. Zhang, C. Hu, S. Yang, *Small Methods* **2020**, *4*, 1900552.
- [33] E. Mosconi, F. De Angelis, *ACS Energy Lett.* **2016**, *1*, 182.
- [34] C. Li, A. Guerrero, S. Huettner, J. Bisquert, *Nat. Commun.* **2018**, *9*, 5113.
- [35] L. Bertoluzzi, C. C. Boyd, N. Rolston, J. Xu, R. Prasanna, B. C. O'Regan, M. D. McGehee, *Joule* **2020**, *4*, 109.
- [36] L. Bertoluzzi, R. A. Belisle, K. A. Bush, R. Checharoen, M. D. McGehee, B. C. O'Regan, *J. Am. Chem. Soc.* **2018**, *140*, 12775.
- [37] Y. Cheng, H. W. Li, J. Qing, Q. D. Yang, Z. Guan, C. Liu, S. H. Cheung, S. K. So, C. S. Lee, S. W. Tsang, *J. Mater. Chem. A* **2016**, *4*, 12748.
- [38] Y. Zhou, H. Sternlicht, N. P. Padture, *Joule* **2019**, *3*, 641.
- [39] I. M. Pavlovets, M. C. Brennan, S. Draguta, A. Ruth, T. Moot, J. A. Christians, K. Aleshire, S. P. Harvey, S. Toso, S. U. Nanayakkara, J. Messinger, J. M. Luther, M. Kuno, *ACS Energy Lett.* **2020**, *5*, 2802.
- [40] N. Wu, D. Walter, A. Fell, Y. Wu, K. Weber, *J. Phys. Chem. C* **2020**, *124*, 219.
- [41] N. E. Courtier, J. M. Cave, A. B. Walker, G. Richardson, J. M. Foster, *J. Comput. Electron.* **2019**, *18*, 1435.
- [42] A. Walsh, D. O. Scanlon, S. Chen, X. G. Gong, S. H. Wei, *Angew. Chem., Int. Ed.* **2015**, *54*, 1791.
- [43] N. Wu, Y. Wu, D. Walter, H. Shen, T. Duong, D. Grant, C. Barugkin, X. Fu, J. Peng, T. White, K. Catchpole, K. Weber, *Energy Technol.* **2017**, *5*, 1827.
- [44] J. M. Cave, N. E. Courtier, I. A. Blakborn, T. W. Jones, D. Ghosh, K. F. Anderson, L. Lin, A. A. Dijkhoff, G. J. Wilson, K. Feron, M. Saiful Islam, J. M. Foster, G. Richardson, A. B. Walker, *J. Appl. Phys.* **2020**, *128*, 184501.
- [45] J. Thiesbrummel, V. M. Le Corre, F. Peña-Camargo, L. Perdigón-Toro, F. Lang, F. Yang, M. Griseck, E. Gutierrez-Partida, J. Warby, M. D. Farrar, S. Mahesh, P. Caprioglio, S. Albrecht, D. Neher, H. J. Snaith, M. Stolterfoht, *Adv. Energy Mater.* **2021**, *11*, 2101447.
- [46] J. Diekmann, P. Caprioglio, M. H. Futscher, V. M. Le Corre, S. Reichert, F. Jaiser, M. Arvind, L. P. Toro, E. Gutierrez-Partida, F. Peña-Camargo, C. Deibel, B. Ehrler, T. Unold, T. Kirchartz, D. Neher, M. Stolterfoht, *Sol. RRL* **2021**, *5*, 2100219.
- [47] S. N. Habisreutinger, N. K. Noel, H. J. Snaith, *ACS Energy Lett.* **2018**, *3*, 2472.
- [48] D. H. Kang, N. G. Park, *Adv. Mater.* **2019**, *31*, 1805214.
- [49] J. J. Yoo, G. Seo, M. R. Chua, T. G. Park, Y. Lu, F. Rotermund, Y. K. Kim, C. S. Moon, N. J. Jeon, J. P. Correa-Baena, V. Bulović, S. S. Shin, M. G. Bawendi, J. Seo, *Nature* **2021**, *590*, 587.
- [50] H. J. Snaith, A. Abate, J. M. Ball, G. E. Eperon, T. Leijtens, N. K. Noel, S. D. Stranks, J. T. W. Wang, K. Wojciechowski, W. Zhang, *J. Phys. Chem. Lett.* **2014**, *5*, 1511.
- [51] J. Kniepert, I. Lange, N. J. van der Kaap, L. J. A. Koster, D. Neher, *Adv. Energy Mater.* **2014**, *4*, 1301401.
- [52] N. Tripathi, M. Yanagida, Y. Shirai, T. Masuda, L. Han, K. Miyano, *J. Mater. Chem. A* **2015**, *3*, 12081.
- [53] I. Zimmermann, P. Gratia, D. Martineau, G. Grancini, J. N. Audinot, T. Wirtz, M. K. Nazeeruddin, *J. Mater. Chem. A* **2019**, *7*, 8073.
- [54] J. H. Heo, D. H. Song, H. J. Han, S. Y. Kim, J. H. Kim, D. Kim, H. W. Shin, T. K. Ahn, C. Wolf, T.-W. Lee, S. H. Im, *Adv. Mater.* **2015**, *27*, 3424.
- [55] M. Stolterfoht, P. Ca, prioglio, C. M. Wolff, J. A. Márquez, J. Nordmann, S. Zhang, D. Rothhardt, U. Hörmann, Y. Amir, A. Redinger, L. Kegelmann, F. Zu, S. Albrecht, N. Koch, T. Kirchartz, M. Saliba, T. Unold, D. Neher, *Energy Environ. Sci.* **2019**, *12*, 2778.
- [56] I. Levine, P. K. Nayak, J. T.-W. Wang, N. Sakai, S. Van Reenen, T. M. Brenner, S. Mukhopadhyay, H. J. Snaith, G. Hodes, D. Cahen, *J. Phys. Chem. C* **2016**, *120*, 16399.
- [57] O. J. Sandberg, J. Kurpiers, M. Stolterfoht, D. Neher, P. Meredith, S. Shoaee, A. Armin, *Adv. Mater. Interfaces* **2020**, *7*, 2000041.
- [58] L. Perdigón-Toro, L. Q. Phuong, S. Zeiske, K. Vandewal, A. Armin, S. Shoaee, D. Neher, *ACS Energy Lett.* **2021**, *6*, 557.
- [59] M. H. Futscher, M. K. Gangishetty, D. N. Congreve, B. Ehrler, *J. Chem. Phys.* **2020**, *152*, 044202.
- [60] O. Almora, C. Aranda, E. Mas-Marzá, G. Garcia-Belmonte, *Appl. Phys. Lett.* **2016**, *109*, 173903.
- [61] I. Zarazua, J. Bisquert, G. Garcia-Belmonte, *J. Phys. Chem. Lett.* **2016**, *7*, 525.
- [62] H. S. Duan, H. Zhou, Q. Chen, P. Sun, S. Luo, T. Bin Song, B. Bob, Y. Yang, *Phys. Chem. Chem. Phys.* **2014**, *17*, 112.
- [63] K. Miyano, N. Tripathi, M. Yanagida, Y. Shirai, *Acc. Chem. Res.* **2016**, *49*, 303.